Check for updates

Received: 20 September 2023 | Revised: 30 November 2023 | Accepted: 7 December 2023

DOI: 10.1002/hyp.15060

RESEARCH ARTICLE

WILEY

Microstructural characterization of depth hoar and ice-crust layers using a micro-CT, and hypothesis of ice-crust formation under a thunderstorm

Yuan Li[1] | Ciao Fu[2] | Kaitlin Keegan[3] | Junhua Yang[4] | Gang Huang[5,6] | Ian Baker[1]

[1]Thayer School of Engineering, Dartmouth College, Hanover, New Hampshire, USA

[2]School of Earth Sciences, Yunnan University, Kunming, China

[3]Department of Geological Sciences & Engineering, University of Nevada, Reno, Reno, Nevada, USA

[4]State Key Laboratory of Cryospheric Sciences, Northwest Institute of Eco-Environment and Resources, Chinese Academy of Sciences, Lanzhou, China

[5]State Key Laboratory of Numerical Modeling for Atmospheric Sciences and Geophysical Fluid Dynamics, Institute of Atmospheric Physics, Chinese Academy of Sciences, Beijing, China

[6]Laboratory for Regional Oceanography and Numerical Modeling, Qingdao National Laboratory for Marine Science and Technology, Qingdao, China

Correspondence
Yuan Li and Ian Baker, Thayer School of Engineering, Dartmouth College, Hanover, NH, USA.
Email: liyuan0614@163.com; ian.baker@dartmouth.edu

Funding information
National Science Foundation of USA Arctic Natural Science, Grant/Award Number: 1603239; National Science Foundation of China, Grant/Award Number: 42071096; State Key Laboratory of Cryospheric Science, Grant/Award Number: SKLCS-ZZ-2022; National Key R & D Program of China, Grant/Award Number: 2018YFA0605904

Abstract

The microstructural features typical of depth hoar and ice-crust layers in both blocks of snow and a firn core that were extracted at Summit, Greenland (72°35′ N, 38°25′ W) in June, 2017 have been characterized using x-ray microcomputed tomography (micro-CT). In the depth hoar, the density is much lower, and the porosity, pore sizes, and specific surface area (SSA) are greater than those in adjacent layers. In the ice-crusts, the density and the particle size are greater, and the porosity, pore size, and SSA are less than those in adjacent layers. Note that the mean structure thickness in the depth hoar was greater than that in adjacent layers, but that increase was simply related to the one- or two-dimension ice crystals, that is, needle-like or plate-like structures, being included in the measurements for depth hoar. Using related micro-structural parameters derived from the micro-CT data, we propose a model based on refreezing of pre-melted water (PMW) droplets electrostatically-transported by the electric field between thunderclouds and the ice sheet created by a thunderstorm that describes the processes of the ice-crust formation (ICF). Whether the ice-crust forms with depth hoar depends on both the kinetic energy from the PMW droplets and the latent heat liberated from the freezing of the PMW. This work is the first to build the relationship between the atmosphere and ice sheets by a thunderstorm. Finally, we provide an experimental geophysics-based method through the ICF under laboratory conditions to learn more about the interaction between atmospheric electrodynamics and thermodynamics.

KEYWORDS
atmosphere, depth hoar, ice, ice sheet, snow, thunderstorm

1 | INTRODUCTION

An interesting recent report noted that ice-crusts have a nearly 50% probability of co-existing with depth hoar in Antarctica (56%) and in Greenland (43%), in which the depth hoar was usually located within 2–30 mm beneath the crusts (Weinhart et al., 2021). Depth hoar layers are typically sub-centimetre to a few centimetres thick with sharp basal contacts (Giddings & LaChapelle, 1962). They result from water vapour sublimation and subsequent re-deposition in nearby low-density firn subjected to a steep temperature gradient (≥10°C/m) in layers near the surface of the snow cover. Depth hoar crystals are usually characterized by comparatively large, weakly-bonded grains,

© 2023 John Wiley & Sons Ltd.

which are cupped, scrolls, faceted, or hollow. The physical properties of depth hoar depend on the conditions under which they form, that is, the temperature gradient, the water vapour pressure, and the diffusion rate of vapour in the air (Giddings & LaChapelle, 1962; Hobbs, 1974). There has been a long-standing controversy on the importance of water vapour transport and heat flux in depth hoar formation (Li & Baker, 2022a and references therein). In contrast, the physical processes of ice-crust formation (ICF) have seldom been discussed (Battle et al., 2011; Das & Alley, 2005; Fegyveresi et al., 2018; Mitchell et al., 2015; Sommer, Lehning, et al., 2018; Sommer, Wever, et al., 2018; Weinhart et al., 2021). The ice-crust layers are harder and denser (lower porosity) than adjacent snow, and are present as a well-defined layer in a firn core. They are typically thin and has a roughly constant thickness ≤1 mm with the rare thicker crust up to 2 mm thick (Weinhart et al., 2021). The *c*-axes of the grains in the ice-crust are approximately normal to the surface of the ice sheet, probably due to the effect of capillary waves (Tang et al., 2020). Clearly, they are quite different to ice lenses, which form via a wet process originating from the melting of firn. An ice lens is less defined and has a varying thickness. Often a lens does not cross the entire core. The low density of depth hoar is commonly attributed to mass loss resulting from water sublimation. Conversely, the high density of an ice-crust is attributed to mass gain. The ice-crusts are different to sedimentary layers of firn stratification (Fourteau et al., 2019) arising from the deposit of wind-blown continental dust, sea salt (Alley, 2000), and drifting snow in blizzards (Weinhart et al., 2021). The initial sedimentary layers are less likely to survive during firn densification. The ice-crusts are also different to wind-crusts which are thin layers of hard snow with high mass density produced by wind erosion (Faria et al., 2018; Weinhart et al., 2021). The frequency of the wind-crust formation is high due to prevailing storm events in polar areas. A bubble-free or nearly bubble-free glazed surface crust accompanying surface hoar was reported by Fegyveresi et al. (2018), the formation of which was proposed to be primarily by condensation of water vapour moving upwards in snow deposited from storm events in the uppermost surface of ice sheets in summertime. The surface hoar was suggested to be formed by warm vapour flowing through cracked crusts (Fegyveresi et al., 2018; Mitchell et al., 2015). In wind-packing experiments, the deposition of snow was a necessary but not a sufficient condition for ICF, as hardening of new snow during erosion was not observed (Sommer, Lehning, et al., 2018). While Weinhart et al. (2021) could not establish a direct dependence between crust formation and events with a high wind speed, especially in wind scour areas over the Antarctic continent, Sommer, Wever, et al. (2018) suggested that the higher snow hardness in Antarctica than that obtained in their wind tunnel experiments was most likely due to higher wind speeds in Antarctica. However, the wind effect cannot explain the typical characteristics of ice-crusts, for example, their thickness, rapidity of formation, and the correlation of the frequency of ICF with the accumulation rate (Weinhart et al., 2021). Additionally, these characteristics cannot be explained both by the common energy budget as bulk meltwater in insolation, or by collision of ice particles during a storm in the polar region. Thus, there has yet to be a clear explanation of the process of mass gain. An additional interesting question is why an ICF is sometimes present along with depth hoar. The layered character of both depth hoar and ice-crust layers in a snowpack plays an important role in several phenomena. First, the cohesive strength between these features and the surrounding layers influences the mechanical behaviour of snow, including its flow law. Second, they affect the local thermal distribution across the interfaces between the layers and the adjacent snow (Winarto et al., 2015). Third, the mass density gradient at the layer boundaries impacts the electromagnetic response, for example, the remote sensing reaction to horizontally-polarized microwave radiation (Winebrenner et al., 2001). Fourth, the variable gas permeability at the interfacial layer modifies the diffusion of atmospheric gases through the firn, which determines the age difference between the air trapped in bubbles at pore close-off, and the surrounding ice. This, in turn, affects the interpretation of paleoclimate information archived in ice cores. Building on the relevant studies in the literature, both the effects of kinetic and thermal energies should be combined in considering ICF. To that end, through the reconstruction of the 3-D microstructure of depth hoar and ice-crust layers using the non-destructive technique of x-ray micro-computed tomography (micro-CT), we propose a model based on refreezing of electrostatically-transported pre-melted water (PMW) droplets to understand the physical processes of the ICF with and without depth hoar. This work aimed to fill in the gaps in knowledge with pertinent quantitative studies on ICF.

2 | SAMPLES AND METHODS

Cuboidal blocks of snow of dimensions 100×100 mm and 170–190 mm long (cut sequentially from the surface down to 2 m depth), and an ~80 mm diameter, 80 m long cylindrical firn core (from below 2 m) were extracted at Summit, Greenland (72°35′ N, 38°25′ W) in June, 2017, and transported to the US Army Corps of Engineers Cold Region Research Engineering Laboratory, Hanover, NH, where they were stored at −30°C. Using a hole saw, two cylindrical samples containing depth hoar layers (Depth Hoar-S1: ~17.5 mm diameter and ~34 mm high, and Depth Hoar-S2: ~21.5 mm diameter and ~21 mm high) were cut from the snow blocks at depths of 47 and 68 cm, while two cylindrical samples containing ice-crust layers (Ice-Crust-30: ~21.5 mm diameter and ~22 mm high, and Ice-Crust-70: ~19.5 mm diameter and ~17 mm high) were cut from the firn core from depths of 30 and 70 m (Figure 1). Immediately prior to examination in a micro-CT, the samples were completely enveloped with plastic wrap to minimize sublimation and stored in the Ice Research Laboratory at Dartmouth College at a temperature of −10°C for 2 days to achieve thermal equilibrium.

The samples were scanned using a Skyscan 1172 micro-CT, which was housed in a freezer room at −18°C. This cold room temperature enabled a temperature of −10°C to be maintained inside the chamber of the micro-CT, which warms during scanning due to the heat produced from x-ray generation. An accelerating voltage of 40 kV was used at a current of 250 μA to provide good contrast for imaging

10991085, 2023, 12, Downloaded from https://onlinelibrary.wiley.com/doi/10.1002/hyp.15060 by Institution Of Atmospheric Physics, Wiley Online Library on [27/01/2024]. See the Terms and Conditions (https://onlinelibrary.wiley.com/terms-and-conditions) on Wiley Online Library for rules of use; OA articles are governed by the applicable Creative Commons License

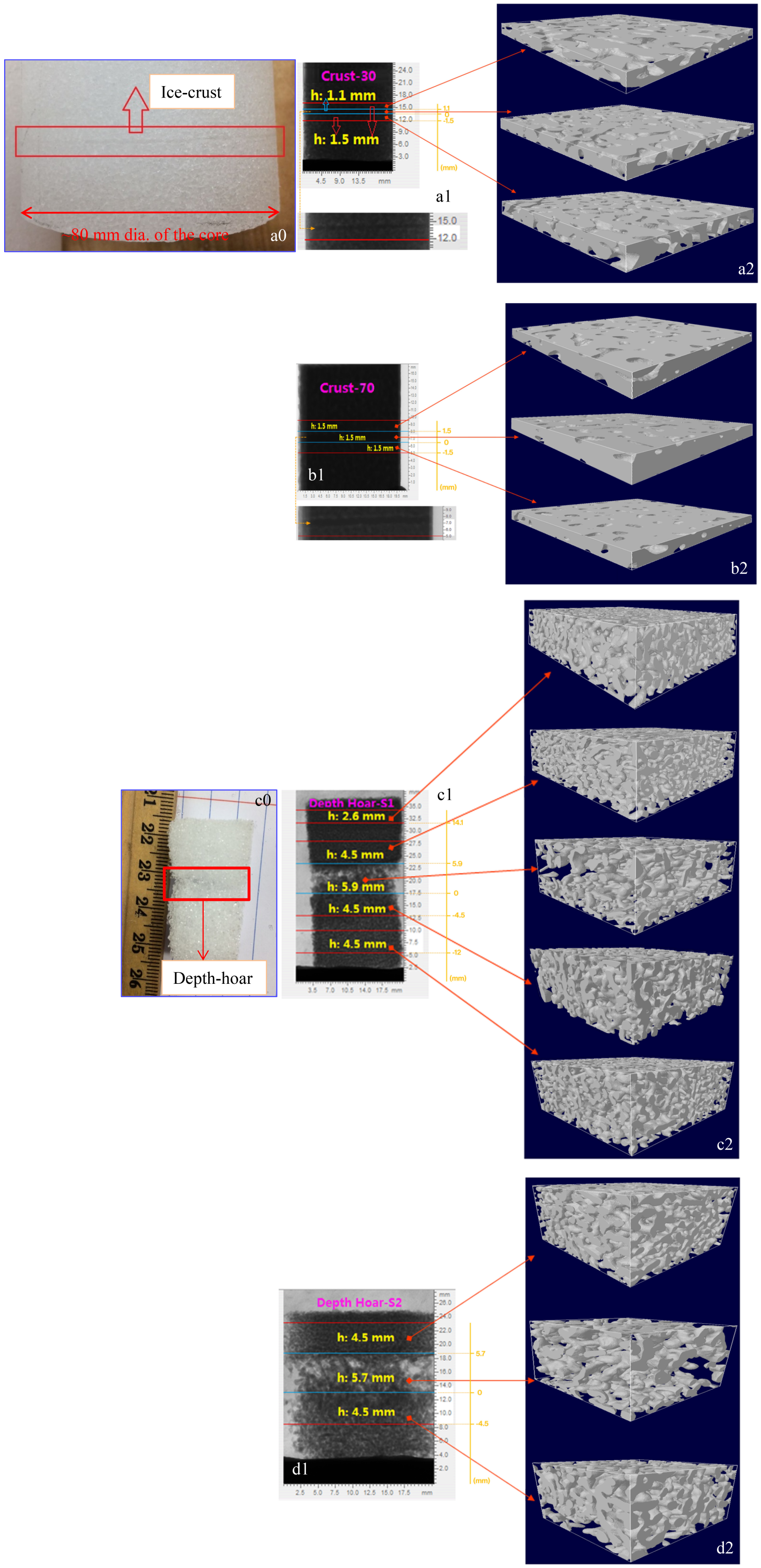

FIGURE 1 Sample photos (a0 and c0), optical micrographs (a1, b1, c1, and d1), and 3D micro-CT reconstruction images (a2, b2, c2, and d2). (a) is from the Depth Hoar-S1 sample. (b) is from the Depth Hoar-S2 sample. (c) is from the Ice-Crust-30 sample. (d) is from the Ice-Crust-70 sample. Each optical micrograph section and its 3D reconstruction image are connected by red double arrows. The computed sample height (h) is numbered in yellow, and the cross-section of computed sample is 6×6 mm^2. The segments between two dark blue lines are the depth hoar or the ice-crust, otherwise they are layers above or below the depth hoar or the ice-crust. To highlight the ice-crust layer in optical micrograph, the contrast of the original image has been indicated by a dotted orange arrow. The 0 position of sample indicates the position of bottom end of either the depth hoar or ice-crust segment. The relative displacements to the 0 position of sample in the abscissa axis (Figure 2) are denoted as the orange ordinate in mm scale.

snow and firn. The image pixel size was set to 17 μm. Scans were performed every 0.7° up to a 180° rotation. Each micro-CT reconstruction consists of 257 projection images. Because ice and air have very different x-ray attenuation coefficients, a constant threshold identifying the ice and air phases was used throughout. NRecon software was used to transform a stack of projection images into grey-scale images.

10991085, 2023, 12, Downloaded from https://onlinelibrary.wiley.com/doi/10.1002/hyp.15060 by Institution Of Atmospheric Physics, Wiley Online Library on [27/01/2024]. See the Terms and Conditions (https://onlinelibrary.wiley.com/terms-and-conditions) on Wiley Online Library for rules of use; OA articles are governed by the applicable Creative Commons License

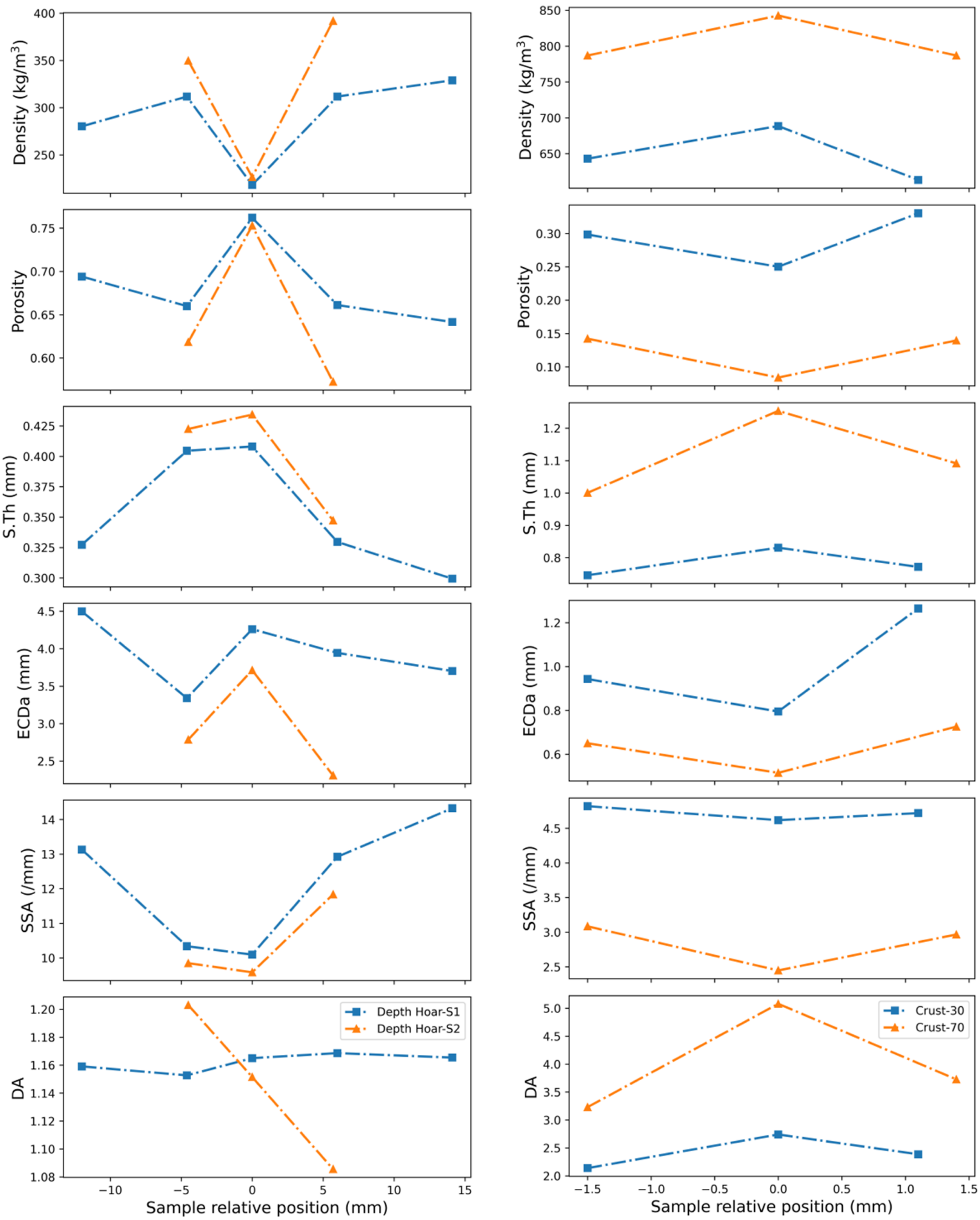

FIGURE 2 Plots of the microstructural parameters and the relative position in the sample as denoted in the orange ordinate in mm in Figure 1. The standard deviation of the microstructural parameters measured using the micro-CT is smaller than the symbols indicating the data.

After thresholding, binary images were obtained using CTAn software, in which artefacts smaller than 25 voxels (a 3-D pixel) were removed. The cuboidal Volume of Interest (VOI; the cross-section is 6 × 6 mm^2 with different heights from 1.1–5.9 mm) was taken from near the centre of the specimen to minimize both the cut and edge effects. The standard deviation of each parameter calculated from the images was from three VOIs. That is, the height of VOI was moved up and down aligning with the vertical axis of the specimen by ~0.5 mm. The microstructural parameters of interest from the micro-CT data are the density (ρ-kg m^{-3}), the mean structure thickness (S.Th-mm), the

10991085, 2023, 12, Downloaded from https://onlinelibrary.wiley.com/doi/10.1002/hyp.15060 by Institution Of Atmospheric Physics, Wiley Online Library on [27/01/2024]. See the Terms and Conditions (https://onlinelibrary.wiley.com/terms-and-conditions) on Wiley Online Library for rules of use; OA articles are governed by the applicable Creative Commons License

area-equivalent circle diameter (ECDa-mm), the specific surface area (SSA-mm^{-1}), the porosity (φ), and the degree of anisotropy (DA). For the definition of ρ, S.Th, ECDa, SSA, and φ, see elsewhere (Li & Baker, 2021; Li & Baker, 2022a, 2022b and references therein). The DA is a measure of alignment or 3-D symmetry in the enclosed region or VOI containing the ice matrix and the air phase. The following algorithms on the image processing are sequentially run through the mean intercept length (MIL) analysis: the visualization of the 3-D distribution of MIL as an ellipsoid, the statistical fitting of ellipsoid to the MIL pin-cushion 3-D polar plot, and the calculation of maximum and minimum eigenvalues describing the anisotropy ellipsoid. Finally, the value of DA is traditionally expressed by the ratio of the maximum eigenvalue to the minimum eigenvalue. The degree of anisotropy in porous materials increases with increasing values of DA. That is, DA $= 1$ indicates a totally isotropic material, while DA $= \infty$ represents a fully anisotropic material (http://www.skyscan.be). It is worth highlighting that the SSA characterizes the thickness and complexity of the firn microstructure. The change in SSA is also indicative of changes in the energy of the ice surfaces. In other words, its decrease is related to temperature-activated pressureless sintering (Li et al., 2023), whereas the increase is associated with temperature-gradient metamorphism (Li & Baker, 2022a).

3 | RESULTS AND DISCUSSION

3.1 | Changes in microstructure

The 3-D reconstructions derived from the micro-CT data for the four samples of interest are shown in Figure 1. The differences between the depth hoar and adjacent layers are clearly visible, while the differences between the ice-crust and adjacent layers cannot be readily recognized by visual inspection of the micro-CT reconstructions. As might be expected, the ice-crust that initially formed on the surface of ice sheets has an apparent microstructural difference from the underlying snow. The subsequent microstructural difference between the ice-crust and adjacent layers, including the overlying snow or firn later, weakens with increasing depth owing to rapid sintering of snow or firn during densification, for example, changes in S.Th and SSA (Figure 2). Further, the ice-crusts can be preserved and densified from the surface through the bubbly ice above the zone of mass loss (non-ablation zone; Fegyveresi et al., 2018; Weinhart et al., 2021). This is evidenced by an increase of both the S.Th and the density of the ice-crust from 30 to 70 m (Figure 2), in which the pressure sintering of the snow from the firn overburden occurred. In contrast, depth hoar usually forms and remains in the shallow snow depths, making it easier to identify the microstructural differences between the depth hoar and adjacent layers. Incidentally, that the depth hoar is less likely to survive to greater depths is attributed to the weaker temperature gradient. Note that the ice-crusts tend to have a slight inclination with respect to the stratigraphy (Figure 1a0), and, hence, their real thickness may be overestimated during the micro-CT measurement. Both the depth hoar and ice-crust with their adjacent layers are well identified by changes in microstructural parameters of interest against the sample relative position in Figure 2, for example, the density of depth hoar is less, and its porosity is greater than that of adjacent layers, and vice versa for the ice-crust layer.

It is worth highlighting that S.Th in the depth hoar is greater than that for adjacent layers, which is consistent with the increase in ice particle size during the formation of the depth hoar. This apparent increase is because only one- or two-dimensional ice particles, that is, needle-like or plate-like structures are measured for the depth hoar (Li & Baker, 2022a). That is, the values of S.Th in the depth hoar may be biased on the preferred growth face(s) observed with the micro-CT. Correspondingly, the values of SSA in these samples may also exhibit an apparent decrease by virtue of using the same algorithm for the micro-CT reconstruction. In contrast, the low values of SSA observed in the ice-crust layers are realistic and reflect the consolidation of firn. However, the abnormally high value of ECDa in the Depth Hoar-S1 sample at the -12 mm position is probably due to the high structural heterogeneity in the small VOI. The depth hoar and adjacent layers have similar quasi-isotropic structures, especially from Depth Hoar-S1, where the values of DA are slightly greater than 1. The values of DA from the adjacent layers for Depth Hoar-S2 fluctuated between 1.09 and 1.2, but they are still close to 1, which is representative of isotropic material. This quasi-isotropic structure may be related to the open void structure predominating in both depth hoar and snow. It is important to note that the values of DA for Ice-Crust-30 and Ice-Crust-70 are 2.74 and 5.08, respectively, which are greater than that for the depth hoar. Figure 2 shows that the deviation of 21.9% and 12.8% in the above and below adjacent layers from 2.74 for the Ice-Crust-30 sample, while the values are 36.4% and 26.6% from 5.08 for the Ice-Crust-70 sample. Clearly, these deviations are greater than 4.2%–5% or less in adjacent layers from the depth hoar. That is, the degree of anisotropy in the ice-crusts is higher than that in the depth hoar, and the variability in the degree of anisotropy around the ice-crust layer is also higher than that around the depth hoar layer. These changes in DA imply that the layered structure difference between the depth hoar and ice-crusts is due to the different mechanisms of their formation. Interestingly, the value of the DA for the ice-crust is greater than that for adjacent firn layers, and the value of DA and the difference in DA between the ice-crust and adjacent layers for the Ice-Crust-70 sample are greater than that for the Ice-Crust-30 sample. These changes in DA mean that both the degree of anisotropy and the variability in DA increase with increasing density (depth), likely owing to the less uniform distribution of pores at greater depths with lower porosity. This is because uneven sintering occurred during post-deposition which may be due to the effects of impurities and dust deposited in the ice-crust layer.

3.2 | Model architecture

We note that the PMW arises at both the interface of ice particles and the grain boundaries primarily via three routes: (1) the

10991085, 2023, 12, Downloaded from https://onlinelibrary.wiley.com/doi/10.1002/hyp.15060 by Institution Of Atmospheric Physics, Wiley Online Library on [27/01/2024]. See the Terms and Conditions (https://onlinelibrary.wiley.com/terms-and-conditions) on Wiley Online Library for rules of use; OA articles are governed by the applicable Creative Commons License

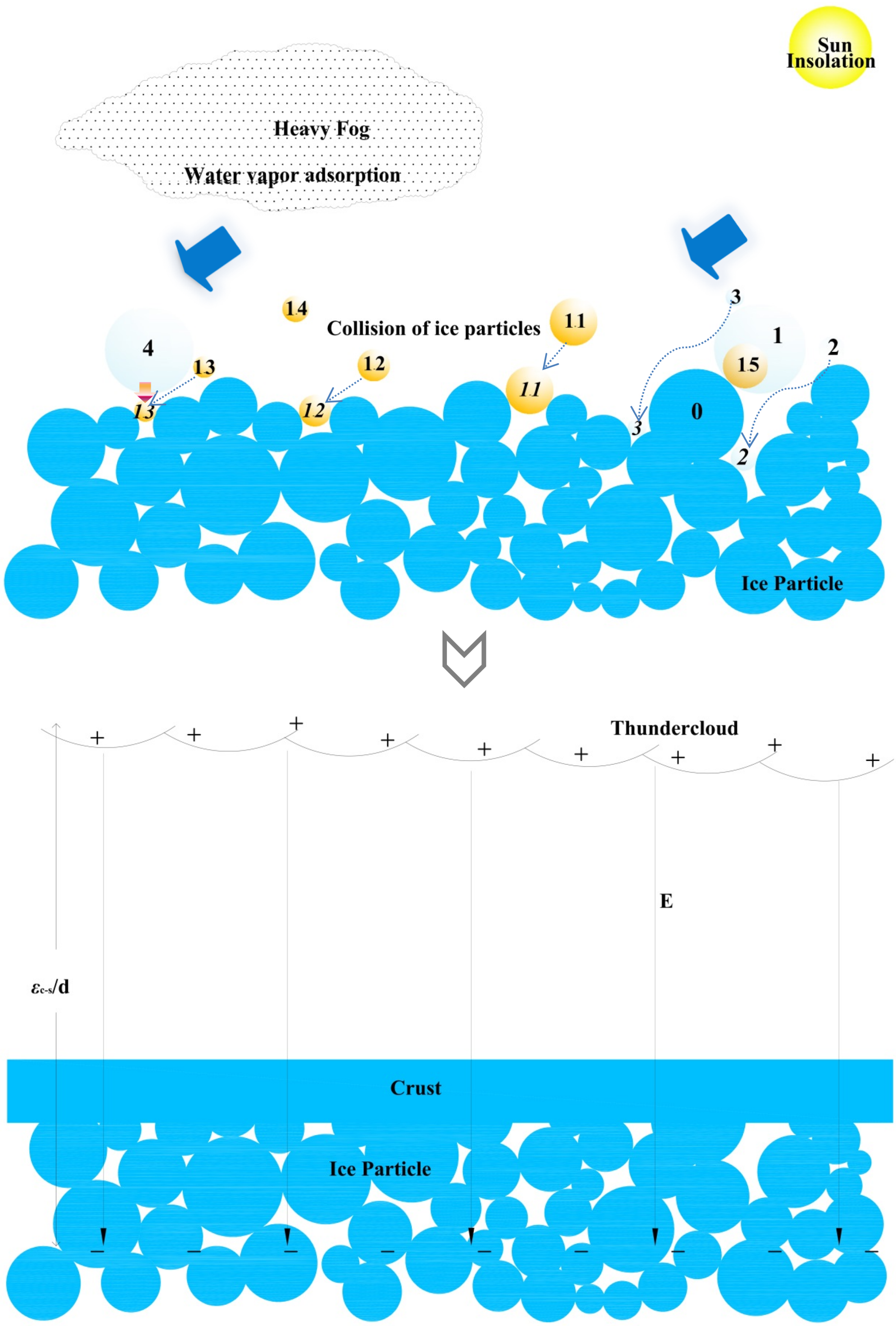

FIGURE 3 Schematic model of ice-crust formation showing the pre-melted water produced by insolation of the Sun in summertime, the collision of ice particles in storms, and the adsorption of polarized vapour water molecules in heavy fog (upper panel). The ice-crust formed by refreezing of pre-melted water droplets agglomerated in the electric filed by a thunderstorm (lower panel). Both the fragmentized ice-particles (the orange particles numbered 1.1, 1.2, 1.3, and 1.4), which originate from a drifting large parent particle (the light blue particle numbered 1) that impact other similar- or larger-sized particles (the blue particle numbered 0; assuming that the 0 particle is intact during impacting) in high speed wind (the dark blue arrows), and the drifting small ice-particles (the light blue particles numbered 2 and 3) fill the porous surface (the particles numbered by italic 1.1, 1.2, 1.3, 2, and 3). This process of the impact compaction not only produces PMW, but stabilizes the surface of ice sheet to favour for the ICF, for example, the large particle 4 is falling onto but does not impact the small particle 1.3 in the gradient red arrow. Note that the retained orange particles numbered 1.5 from a parent particle 1 after impacting is likely bonded directly to the particle numbered 0 by freezing of meltwater. The blue solid circle indicates the granular ice-particle, the blue rectangular block indicates the ice-crust with a thickness of around single mean particle size. The depth-hoar formation is not shown. Note that these meteorological conditions including insolation, storms, heavy fog, or a thunderstorm do not need to be met simultaneously.

temperature effect from insolation of the Sun in summertime (Fegyveresi et al., 2018; Weinhart et al., 2021), even at temperatures as low as a few tens of degrees below the bulk melting point (Dash et al., 2006), (2) the heat from the collision of ice particles during storm events (Dash et al., 2006; Sommer, Lehning, et al., 2018; Szabo & Schneebeli, 2007), and (3) the adsorption of polarized vapour water molecules in heavy fog towards the charged surface of ice sheets resulting from the friction of wind (see the details in the caption of Figure 3). We also note that water molecules adsorbed on the crystal lattice are moveable (Pfalzgraff et al., 2011; Vrbka & Jungwirth, 2005), a feature of which is unrelated to the shear rate and direction at the ice–water interface (Louden & Gezelter, 2017).

Prior to developing a model, we made the following endeavour to explain the ICF. (1) A super-high differential pressure between the surface and subsurface of ice sheets instantly drives the PMW droplets or vapour upward to the surface of ice sheets. In fact, such super-low pressure is less likely to take place at the near-surface of ice sheets because of the presence of the air flow. (2) Capillary action drives the PMW droplets upward to the surface of ice sheets, where the height of the water column, h, rises only to 50 mm or less

10991085, 2023, 12, Downloaded from https://onlinelibrary.wiley.com/doi/10.1002/hyp.15060 by Institution Of Atmospheric Physics, Wiley Online Library on [27/01/2024]. See the Terms and Conditions (https://onlinelibrary.wiley.com/terms-and-conditions) on Wiley Online Library for rules of use; OA articles are governed by the applicable Creative Commons License

10991085, 2023, 12, Downloaded from https://onlinelibrary.wiley.com/doi/10.1002/hyp.15060 by Institution Of Atmospheric Physics, Wiley Online Library on [27/01/2024]. See the Terms and Conditions (https://onlinelibrary.wiley.com/terms-and-conditions) on Wiley Online Library for rules of use; OA articles are governed by the applicable Creative Commons License

TABLE 1 Parameters used in the models.

Symbol	Quantity	Value
A_c	The area of the ice-crust of interest	1 m^2
h_c	The thickness of ice-crust of interest	1 mm
m_c	The mass of ice-crust of interest	kg
$m_{pw\text{-}e}$	The mass of each pre-melted water droplet	kg
ρ_c	The density of the ice-crust of interest	688.5 kg/m^3
ρ_w	The density of liquid water	1000 kg/m^3
j	The number of ice spheres in each layer of snowpack of interest	
$S.Th_{1.1}$	S.Th of snowpack adjacent the ice-crust	0.772 mm
$ECDa_{1.1}$	ECDa of snowpack adjacent the ice-crust	1.265 mm
ℓ	The side-length of each equal-sized cubic in snowpack of interest	2.037 mm
N_A	Avogadro constant	6.022×10^{23}
$N_{pw\text{-}e}$	The number of pre-melted water droplets of interest	
M_c	The number of moles in the ice-crust of interest	mol
Δr	The thickness of pre-melted water on each ice sphere	
r	The radius of ice-sphere un-melted on each ice sphere	
Z	The depth of interest	
m_{wm}	The mass of a water molecule	2.992×10^{-26} kg
$E_{i\text{-}mol}$	Energy of hydrogen bond of 1 molar water molecules in ice I*h*	J/mol
$E_{pw\text{-}mol}$	Energy of hydrogen bond of 1 molar water molecules in liquid water at 0°C and 1 atm	J/mol
$E_{h\text{-}i}$	Energy of hydrogen bond of in ice I*h* of interest	
$E_{h\text{-}pw}$	Energy of hydrogen bond of in liquid water of interest	
ΔE_h	Energy difference of hydrogen bond between ice I*h* and pre-melted water of interest	
$W_{pw\text{-}ek}$	Work done by individual pre-melted water droplet in a displacement of s_k	
$W_{pw\text{-}e}$	Work done by all pre-melted water droplets in *k*th layer snowpack	
W	Total work done from pre-melted water droplets in the depth of interest	
W_L	Latent heat liberating from pre-melted water to ice I*h*	
L_f	Latent heat of fusion of liquid water	3.34×10^5 J/kg
F_{es}	Electrostatic field force	N
$q_{pw\text{-}e}$	Amount of charges for individual pre-melted water droplet	C
$\varepsilon_{c\text{-}s}$	Electric potential difference between a thundercloud and ice sheet	GV/TV
d	The distance between a thundercloud and ice sheet surface (cloud base height)	Km
$\vec{F}$	Resultant force of each pre-melted water droplet	N
a	Acceleration of individual pre-melted droplet under F_{es}	m/s^2
k	The *k*th layer of pre-melted water in the depth of interest	
n	Total number of layers included in the depth of interest	
t_{max}	The maximum travel time from the deepest pre-melted layer to the surface of ice sheets	s

according to Jurin's law, namely, $h = 4\gamma_{w\text{-}a}\cos\theta/\rho_w g ECDa_{1.1}$, where $\gamma_{w\text{-}a}$ is the water–air surface tension, θ is the contact angle of water–ice, g is the acceleration of gravity, for the other variables see Table 1. Clearly, there is insufficient water supply to form the ice-crust of interest ascribed to the large pore size in the snowpack of interest. (3) The difference in saturated vapour pressure between the curved surface of individual PMW droplets, p', and the flat surface of the ice-crust (just before refreezing of a PMW droplet), p, forces the PMW droplets upward to the surface of ice sheets. However, p'/p is too small (<1.115) to offer such forcing since the equivalent spherical radius of a PMW droplet, r_e, is greater than 10 nm using the Kelvin equation, that is, $\ln(p'/p) = 2\gamma_{w\text{-}v}V_{wm}/RTr_e$, where $\gamma_{w\text{-}v}$ is the liquid water–vapour surface tension, V_{wm} is the molar volume of the water, and T is the absolute temperature (Wang, 2014). However, these efforts failed to interpret the ICF.

Alternatively, we note that thunderstorms generate an electric field between the cloud and the ground (ice sheet) (Deierling et al., 2005; Mansell et al., 2005). Thus, we propose a model based on refreezing of PMW droplets electrostatically-transported by the electric field between thunderclouds and the ice sheet produced via a thunderstorm to describe the process of ICF. Further, we divided ice-crusts into two types: the simple ice-crust without depth hoar, and the symbiotic ice-crust with depth hoar. To proceed, the model is based on the following assumptions. (1) The PMW surrounding individual ice spheres is equivalent to an equal-diameter spherical droplet, that is, the PMW droplet (Figure 4). (2) The electric field from cloud-to-ground is uniform, in which the decrement of charges in thunderclouds by electrical neutralization of ground is ignored. (3) The PMW droplets are charged by ionic effects (equivalent to point-charge particle), and then transported electrostatically with vertical acceleration by an electrostatic force upwards to the uppermost surface of ice sheets (the first snow layer, Figure 5). (4) Finally, these droplets come to rest with an inelastic collision, and refreeze instantaneously to the ice just overlying the first of layer snow by self-organizing or self-assembling under the electric field (Lu & Chen, 2021; Winarto et al., 2017). Note that the effect of gravity on a single PMW droplet is balanced by the interfacial force between the PMW and the ice (Figure 4). (5) The energy difference for the hydrogen bonds between PMW and ice I*h* is equal to the sum of kinetic energy (work) of all transported PMW droplets and latent heat liberated from the PMW to ice I*h* in the ice-crust and snowpack of interest. Specifically, the mass of the ice-crust of interest, m_c (Kg), is

$$m_c = A_c \times h_c \times \rho_c \tag{1}$$

where A_c is the area of the ice-crust, and h_c is the thickness of the ice-crust, ρ_c is the density of the ice-crust measured using the micro CT.

Assume that each ice sphere (particle) in the snowpack adjacent to the ice-crust has a PMW film of thickness, Δr, which is distributed

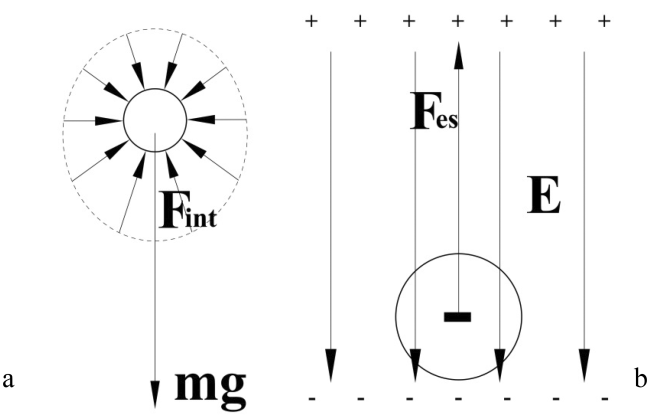

FIGURE 4 Schematic showing mechanical analysis on a pre-melted water droplet. (a) shows the weight, mg, being balanced by the interfacial force between the water and the ice, F_{int}, in the absence of electric field (the shape of a pre-melted water droplet is an eccentric ellipsoid). (b) shows the resultant force being equal to electrostatic force, F_{es}, in a uniform electric field, E, by a thunderstorm between a thundercloud and the ice sheet (the shape of a pre-melted water droplet is an approximately sphere), owing to the balance from other forces as shown in (a). Note that the pre-melted water droplet charged is shown only for a negative charge.

uniformly surrounding an individual equal-sized ice sphere, and the rest (un-melted) radius of individual ice spheres is r. Note that the diameter of each ice sphere before pre-melting is the value of the S.Th measured using the micro CT. Clearly,$r + \Delta r = \frac{1}{2}$S.Th (Figure 5). Also, assume that these ice spheres are uniformly distributed in space. And, hence, the number of ice spheres in each horizontal layer, j, is the same, that is, $j = A_c/\ell^2$, where ℓ is the edge length of a cube, which is equal to the sum of the diameter of an individual ice sphere and its related pore size before pre-melting, that is, $\ell = \text{S.Th} + \text{ECDa}$ (Figure 5). Thus, the mass of an equivalent spherical droplet of PMW on each ice sphere (hereafter abbreviated to PMW droplet), $m_{\text{pw-e}}$, is

$$m_{\text{pw-e}} = \frac{4}{3}\pi\left[(r+\Delta r)^3 - r^3\right]\rho_w = \frac{4}{3}\pi\left[3r^2\Delta r + 3r\Delta r^2 + \Delta r^3\right]\rho_w. \tag{2}$$

where ρ_w is the density of PMW. Clearly, the equivalent radius of PMW droplet, r_e, is $\sqrt[3]{3r^2\Delta r + 3r\Delta r^2 + \Delta r^3}$, which can be regarded as a point charge once charged.

Figure 4 shows that the forces applied on each individual PMW droplet include both the downward gravity, mg, and the interfacial force between the PMW and ice particle, F_{int}. Note that these two forces balance each other to maintain the PMW droplet to adsorb on an ice sphere due to the near-spherical symmetry of PMW surrounding each ice sphere in the absence of electric field. In this case, the resulting force, $\vec{F}$, is in an upward vertical direction, and equal to the electrostatic force, F_{es}, in the presence of the electric field. The uniform electric field between a thundercloud and the ice sheet, E, is given by

$$E = \varepsilon_{\text{c-s}}/d \tag{3}$$

where $\varepsilon_{\text{c-s}}$ and d are the electric potential difference and the average distance between a thundercloud and the ice sheet surface, respectively.

The electrostatic force on each PMW droplet, F_{es}, is given by

$$F_{es} = q_{\text{pw-e}}E \tag{4}$$

where $q_{\text{pw-e}}$ is the electric charge for a PMW droplet. Note that the volume of snowpack beneath the ice-crust to supply PMW to form the ice-crust is equal to the product of the area of the ice-crust of interest and the depth underlying the ice-crust. Let the centre of each PMW droplet be located at the centre of corresponding ice sphere. Clearly, work done by an individual PMW droplet in a vertical displacement of s_k from the kth layer to the surface (1st layer) of ice sheets, $W_{\text{pw-ek}}$, is

$$W_{\text{pw-ek}} = F_{es} \times s_k. \tag{5}$$

Note that $s_k = (k-1) \times \ell$, where the first layer of the surface of ice sheet is used to retain the droplets for the subsequent ICF-as in assumption (3) (Figure 5). Then, work done by all the PMW droplets in the kth layer snowpack is

10991085, 2023, 12, Downloaded from https://onlinelibrary.wiley.com/doi/10.1002/hyp.15060 by Institution Of Atmospheric Physics, Wiley Online Library on [27/01/2024]. See the Terms and Conditions (https://onlinelibrary.wiley.com/terms-and-conditions) on Wiley Online Library for rules of use; OA articles are governed by the applicable Creative Commons License

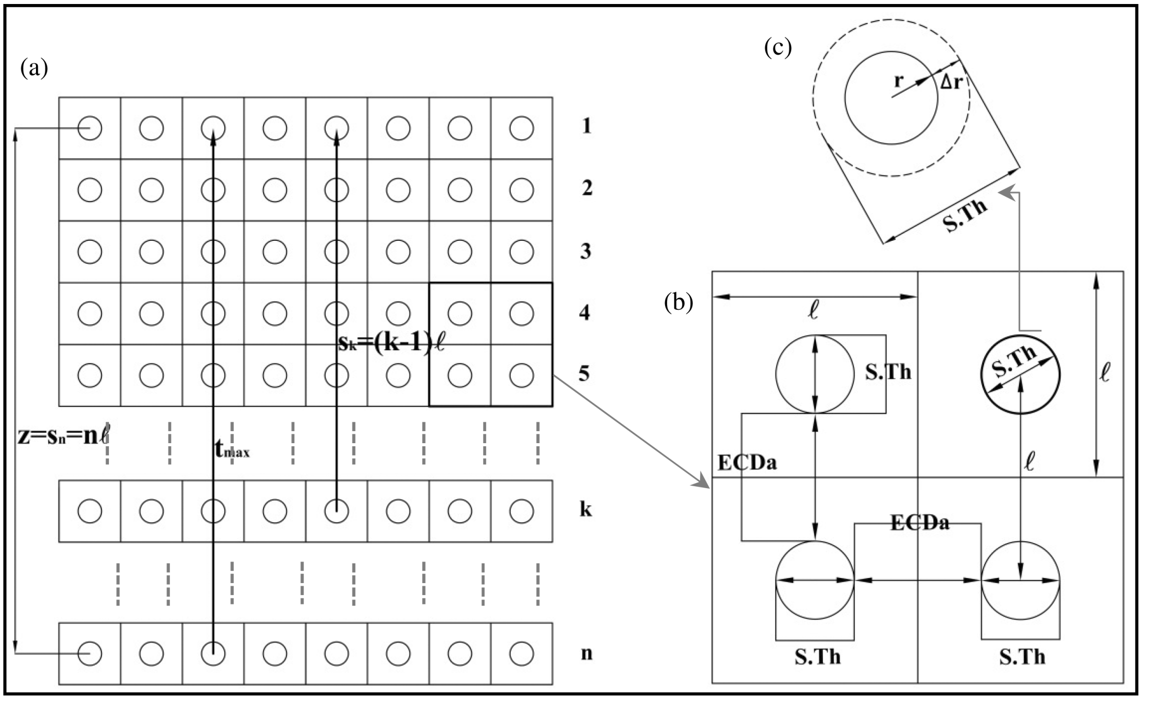

FIGURE 5 Schematic of the geometry used in the model. (a) shows the snowpack adjacent to the upcoming (1st layer) crust. (b) shows enlarged structure of the snowpack, where S.Th and ECDa are illustrated in more detail. (c) shows the structure of pre-melted water surrounding an ice sphere. 1, 2, 3,…, k, and n indicate the layer in snowpack of interest. The side-length of each equal-sized cubic is $\ell = \text{S.Th} + \text{ECDa}$.

$$W_{\text{pw-e}} = j \times F_{\text{es}} \times s_{\text{k}} = (k-1)j\ell F_{\text{es}}. \tag{6}$$

Thus, the total work done by all the PMW droplets in the depth of interest, Z, is

$$W = \sum_{k=1}^{n} (k-1)j\ell F_{\text{es}} = \frac{n(n-1)}{2} j\ell F_{\text{es}}. \tag{7}$$

Since $j = A_{\text{c}}/\ell^2$ and $n = Z/\ell$ (Figure 5), so that

$$W = \frac{A_{\text{c}}\left(Z^2 - Z\ell\right)}{2\ell^3} \times \frac{q_{\text{pw-e}} \times \varepsilon_{\text{c-s}}}{d}. \tag{8}$$

Additionally, the time of the electric field force applied by a thunderstorm should satisfy the time of the deepest PMW droplet in the nth layer travelling to the 1st layer of ice sheets, $t_{\max}$

$$a = 2S_{\text{n}}/t_{\max}^2 = 2Z/t_{\max}^2. \tag{9}$$

Also,

$$a = \frac{\vec{F}}{m_{\text{pw-e}}} = \frac{F_{\text{es}}}{m_{\text{pw-e}}} = \frac{3q_{\text{pw-e}} \times \varepsilon_{\text{c-s}}/d}{4\pi\rho_{\text{w}}\left(3r^2\Delta r + 3r\Delta r^2 + \Delta r^3\right)}. \tag{10}$$

Ignoring both the second- and third-order terms of Δr since $\Delta r < < \text{r}$, Equation (10) can be simplified to

$$a \approx \frac{q_{\text{pw-e}} \times \varepsilon_{\text{c-s}}/d}{4\pi r^2 \Delta r \rho_{\text{w}}}. \tag{11}$$

As a result, the electrostatic force is

$$F_{\text{es}} = \frac{q_{\text{pw-e}} \times \varepsilon_{\text{c-g}}}{d} = \frac{8\pi Z r^2 \Delta r \rho_{\text{w}}}{t_{\max}^2}. \tag{12}$$

Substituting Equation (12) into Equation (8), the total work done by all the PMW droplets in the VOI is

$$W = \frac{4\pi A_{\text{c}} \rho_{\text{w}} r^2 \Delta r \left(Z^3 - Z^2\ell\right)}{\ell^3 t_{\max}^2}. \tag{13}$$

The depth of interest, Z, is calculated as follows. The number of PMW droplets to form the ice-crust is $N_{\text{pw-e}} = \frac{m_{\text{c}}}{m_{\text{pw-e}}} = \frac{A_{\text{c}} \times h_{\text{c}} \times \rho_{\text{c}}}{\frac{4}{3}\pi\rho_{\text{w}}\left(3r^2\Delta r + 3r\Delta r^2 + \Delta r^3\right)}$. Next, the deepest layer in snowpack of interest, n, $n = \frac{N_{\text{pw-e}}}{j} = \frac{3h_{\text{c}} \times \rho_{\text{c}} \times \ell^2}{4\pi\rho_{\text{w}}\left(3r^2\Delta r + 3r\Delta r^2 + \Delta r^3\right)}$. Thereby, $Z = n\ell = \frac{3h_{\text{c}} \times \rho_{\text{c}} \times \ell^3}{4\pi\rho_{\text{w}}\left(3r^2\Delta r + 3r\Delta r^2 + \Delta r^3\right)}$.

We note that the ice-crust from the Ice-Crust-70 specimen is bubbly ice, similar to that observed from Fegyveresi et al. (2018), while the ice-crust observed from the Ice-Crust-30 sample has a density lower than that of bubbly ice. In consideration of the effect of pressure-assisted sintering during post-deposition, the ice-crust newly formed on the surface of ice sheets more likely has the density and S.

10991085, 2023, 12, Downloaded from https://onlinelibrary.wiley.com/doi/10.1002/hyp.15060 by Institution Of Atmospheric Physics, Wiley Online Library on [27/01/2024]. See the Terms and Conditions (https://onlinelibrary.wiley.com/terms-and-conditions) on Wiley Online Library for rules of use; OA articles are governed by the applicable Creative Commons License

10991085, 2023, 12, Downloaded from https://onlinelibrary.wiley.com/doi/10.1002/hyp.15060 by Institution Of Atmospheric Physics, Wiley Online Library on [27/01/2024]. See the Terms and Conditions (https://onlinelibrary.wiley.com/terms-and-conditions) on Wiley Online Library for rules of use; OA articles are governed by the applicable Creative Commons License

Th less than, and the ECDa greater than that from the Ice-Crust-30 sample. Due to the unavailability of data measured in situ from the nascent ice-crust, all the microstructural data used in this model is represented by data from the Ice-Crust-30 specimen measured using the micro-CT (Figure 2). However, there is no loss of generality to verify the validity of the model using these data from the Ice-Crust-30 sample. For other parameters used in the model see Table 1.

3.3 | Model applied in ice-crust formation

3.3.1 | Latent heat liberated from pre-melted water to ice I*h*

The mass of refreezing of the PMW, $m_{pw} = m_c = A_c \times h_c \times \rho_c$. The latent heat liberated from the PMW to ice I*h*, W_L, is $W_L = m_{pw} \times L_f = A_c \times h_c \times \rho_c \times L_f$, where L_f is the latent heat of fusion of liquid water. The area and thickness of the ice-crust of interest are: $A_c = 1\,m^2$, $h_c = 1$ mm. Substituting these values (Table 1) into the above equation, $W_L = 229.96$ kJ.

3.3.2 | Energy difference for the hydrogen bonds between pre-melted water and ice I*h*

A water molecule, on the one hand, binds to four other water molecules by hydrogen bonds in ice I*h*. However, a hydrogen bond is shared between two water molecules (Batista et al., 1998). Clearly, a water molecule includes two hydrogen bonds in ice I*h*. Further, the energy of a hydrogen bond is 0.29 eV = 0.4646×10^{-19} J in ice I*h* (Hobbs, 1974). Thus, the energy of hydrogen bonds in a mole of water molecules in ice I*h* is $E_{mol\text{-}i} = 2 \times 0.4646 \times 10^{-19}\,J \times N_A/mol = 55.96$ kJ/mol. On the other hand, the energy of hydrogen bonds in a mole of water molecules in liquid water at 0°C and 1 atm is $E_{mol\text{-}pw} = 3.69/2 \times 23$ kJ/mol $= 42.44$ kJ/mol, where a water molecule includes 3.69/2 hydrogen bonds on average in liquid water (Jorgensen & Madura, 1985). Note that a hydrogen bond truncated on the surface of both ice crystal and liquid water is considered as a complete hydrogen bond. The number of moles of the water molecules in the ice-crust of interest, M_c, is $M_c = \frac{A_c \times h_c \times \rho_c}{m_{wm} N_A} = 38.21$ mol, where m_{wm} is the mass of a water molecule. As a result, the energy difference of hydrogen bonds between ice I*h* and PMW at 0°C and 1 atm, ΔE_h, is $\Delta E_h = M_c(E_{mol\text{-}i} - E_{mol\text{-}pw}) = 516.6$ kJ.

3.3.3 | Work done by pre-melted water droplets of interest and ice-crust formation

The work done by the PMW droplets of interest, W, was calculated using equation $W = \frac{4\pi A_c \rho_w r^2 \Delta r (Z^3 - Z^2 \ell)}{\ell^3 t_{max}^2}$. The side-length of each equal-sized cubic is ℓ, that is, $\ell = S.Th_{1.1} + ECDa_{1.1} = 2.037$ mm (Figure 5; Table 1), where $S.Th_{1.1}$ and $ECDa_{1.1}$ are from data at 1.1 mm of the Ice-Crust-30 specimen (Figure 2). The depth beneath the ice-crust of interest to supply the PMW, Z, is a dependent of both ℓ and the thickness of the PMW on the individual ice spheres, Δr, that is, $Z = \frac{3h_c \times \rho_c \times \ell^3}{4\pi \rho_w (3r^2 \Delta r + 3r \Delta r^2 + \Delta r^3)}$. The thickness of the PMW layer was estimated to be about several water molecular distances (Baker & Dash, 1989; Fletcher, 1968). Halogen elements enable the quasi-liquid layer in ice to exist down to −40°C with a rapidly reduced thickness as the temperature decreases below the melting point (Wettlaufer, 1999). Letting $\Delta r = S.Th_{1.1}/100$, $\Delta r = S.Th_{1.1}/1000$, and $\Delta r = S.Th_{1.1}/10000$, respectively, Z was calculated to be 0.42, 4.04, and 40.31 m, respectively. Further, let $W = \Delta E_h - W_L = 286.67$ kJ. Consequently, the maximum travel time from the deepest PMW layer, n, to the 1st layer of ice sheets, t_{max}, using equation $W = \frac{4\pi A_c \rho_w r^2 \Delta r (Z^3 - Z^2 \ell)}{\ell^3 t_{max}^2}$, is 0.65, 6.3, and 62.5 ms, respectively. Clearly, t_{max} is less than the average duration of a lighting flash of 425 ms (Zheng et al., 2019), implying that the PMW droplets were most likely electrostatically transported multiple times during lighting. Incidentally, there exists a power dependence of both Z and t_{max} on Δr, that is, $Z = 4.3 \times 10^{-3} \Delta r^{-0.991}$, and $t_{max} = 6.7 \times 10^{-3} \Delta r^{-0.991}$, respectively.

It is important to note that the depth of 0.42 m at Summit is in a zone in which the temperature gradient frequently alternates (Dadic et al., 2008) over a range of timescales from diurnally to seasonally (Bartels-Rausch et al., 2014). Thus, the electric field at this depth may be weakened or offset by the electric potential resulting from the temperature gradient (Hobbs, 1974; Li, 2023), so that the PMW droplets cannot be separated apart from ice spheres to form the ice-crust. However, at depth of ~40 m, it is seemingly hard to ensure that the motion of a PMW droplet through the firn occurs. Nevertheless, the depth of interest to supply the PMW to form the ice-crust is most likely on the scale of metres, accompanied by a time scale of milliseconds, which is in agreement with that from refreezing of the quasi-liquid layer at the contact region by the fast bond formation (Szabo & Schneebeli, 2007). A thin ice-crust formed parallel to the surface of an ice sheet (Figure 3) may be related to capillary waves, which can produce roughness of the surface of the ice-crust on the scale of nanometres (Tang et al., 2020). It is noteworthy that we found the ice-crusts only at the two depths of 30 m (~1913 AD) and 70 m (~1766–1784 AD), meaning the frequency of ICF (the average number of ICF over a year) is as low as 0.0135–0.0154, that is, the ice-crust appears once every 65–74 years, in terms of the chronology data of the GRIP and GISP2 cores (Data is from the Former Centre for Ice and Climate Niels Bohr Institute http://www.iceandclimate.nbi.ku.dk/data/). We note, then, that thunderstorms in Greenland took place on average less than once per year, about once every 10 years north of the Arctic circle, once every 6 years at Laurie Island, South Orkneys (60°44′ S), and once every 2 years at Cumberland Bay, South Georgia (54° S; Brooks, 1925). Additionally, winter thunderstorms near Hong Kong occurred on average once every 6.25 years (Chan et al., 2021). More likely, thunderstorms in Summit, Greenland occur more rarely, for example, once every 65–74 years. In summary, this model explains the typical characteristics of ice-crusts, that is, their thin thickness, and their rapidity and low frequency of formation.

Whether the depth hoar forms with the ice-crust depends on whether both the kinetic energy (work) from the PMW droplets of interest travelling to the surface of the ice sheet, and the latent heat liberating from the PMW to ice I*h* can be removed in time. The symbiotic ice-crust with depth hoar forms by the residual heat underlying the ice-crust, provided that the time of exposure to an effective temperature gradient (≥10 K/m) is long enough (Li & Baker, 2022a). Otherwise, a simple ice-crust forms without depth hoar. Even though the ice-crust formation is linked to thunderstorms, indicative of the occurrence of climate change, whether the ice-crust can be used to reconstruct the climate of the past remains unclear since there is a difference between the nascent ice-crust on the surface of ice sheets and subsequent evolution during post-deposition, for example, the microstructural parameter DA (Section 3.1).

3.4 | Scientific implications and outlook

To investigate the source of electrification for the ICF, we also assessed the electrical effect of drifting snow. The electric field produced by drifting snow near the surface of ice sheets is only 2.5–50 × 10^4 V/m, which is far lower than a value of 9.8 × 10^9 V/m potentially generated under a thunderstorm. This can be used in an estimation of the charge-to-mass ratio of individual snow particles from drifting snow (Gordon & Taylor, 2009; Schmidt & Dent, 1993), assuming that the charge-to-mass ratio of individual PMW droplets, $q_{\text{pw-e}}/m_{\text{pw-e}}$, is equal to the maximum charge-to-mass ratio of 2.08 × 10^{-4} C/kg for individual drifting snow particles reported by Schmidt et al. (1998) ($E = m_{\text{pw-e}}a/q_{\text{pw-e}} = 9.8 \times 10^9$ V/m, where $a = 2Z/t_{\max}^2 = 2.04 \times 10^6\,\text{m/s}^2$). Then, the mass of individual PMW droplets, $m_{\text{pw-e}} = 4\pi r_e^3 \rho_w/3 = 1.44 \times 10^{-9}\,\text{kg}$, and, hence, $q_{\text{pw-e}} = 3 \times 10^{-13}$ C. Thus, the electrical effect of drifting snow is not sufficient to lead to the ICF. Further, the frequency of ICF (Section 0.3.3) is far less than that of the occurrence of snowstorms in the polar region. Thus, we expect that the ICF is less likely related to drifting snow, and more likely related to thunderstorms.

As might be anticipated, laboratory experiments of the ICF facilitates an estimation of related electro-dynamic parameters, for example, F_{es}, and the amount of charges for an individual PMW droplet, $q_{\text{pw-e}}$. Also, the atmospheric electrodynamics and thermodynamics can be unified for the ICF, using the formula $\varepsilon_{\text{c-s}}/d = F_{\text{es}}/q_{\text{pw-e}}$, where $\varepsilon_{\text{c-s}}$ is the electric potential difference from the cloud-to-ground, and d is the cloud-to-ground distance or cloud base height. It is important to note that d also determines two other thermodynamic parameters, that is, the updraft kinetics and the convective available potential energies in thunderstorms (Williams et al., 2005). Here, we define an electro-thermo coefficient, C_{ET} (N/C), as the ratio of F_{es} to $q_{\text{pw-e}}$. C_{ET} can be subdivided into the following three cases. (1) C_{ET} is a constant, for example, $C_{\text{ET}} = 9.8$ N/pC as noted above. This means that $\varepsilon_{\text{c-s}}$ has a linear dependence on d (Figure 6a). (2) C_{ET} is assumed to be a periodic function of d, for example, a sinusoidal equation $\varepsilon_{\text{c-s}} = c + d \times \sin(2\pi \times \omega \times t + \varphi)$ (Figure 6b), where ω is the frequency of the lighting flash, typically 0.0167 flashes/s (Boccippio, 2001), c is the vertical shift with respect to the mid-line of $\varepsilon_{\text{c-s}} = \sin(2\pi \times \omega \times t)$, and φ is the phase in radians. (3) C_{ET} is described by a non-periodic function, which leads to more complex relationships (Figure 6c) than the scenarios in (1) and (2). If F_{es} remains constant, $\varepsilon_{\text{c-s}}/d$ increases with decreasing $q_{\text{pw-e}}$, and the high value of $\varepsilon_{\text{c-s}}/d$ is limited to a small range of $q_{\text{pw-e}}$ (Figure 6c1). If $q_{\text{pw-e}}$ remains constant, $\varepsilon_{\text{c-s}}/d$ increases with increasing F_{es}, and the high value of $\varepsilon_{\text{c-s}}/d$ is still limited to a small range of $q_{\text{pw-e}}$ (Figure 6c1). These changes are also clear in the contour values of $\varepsilon_{\text{c-s}}/d$ (Figure 6c2) projected from Figure 6c1. These imply $\varepsilon_{\text{c-s}}/d$ is highly sensitive to $q_{\text{pw-e}}$, but not to F_{es}. That is, the values on the curved surface of $\varepsilon_{\text{c-s}}/d$ increase rapidly with increasing F_{es} and decreasing $q_{\text{pw-e}}$ in a limited range of low values of $q_{\text{pw-e}}$ (Figure 6c). Note that the positive or negative value of $\varepsilon_{\text{c-s}}$ depends on the direction of electric field from cloud-to-ground (Caranti & Illingworth, 1983; Wang et al., 2018), namely, the charge property in a thundercloud, which is determined by cloud conditions in electrification of thunderstorms, may be varying.

Interestingly, a rising challenge is the atmospheric thermodynamics of thunderstorm formation. Conventionally, thunderstorms originate from the warm and wet convection air. In contrast, winter and polar thunderstorms, which emerge in cool/cold and dry air flow, have been observed increasingly in Japan, Austria, Israel, Hong Kong, and Arctic (Chan et al., 2021; Chen et al., 2021; Diendorfer et al., 2006; Ganot et al., 2007; Holzworth et al., 2021; Torii et al., 2002). These uncommon thunderstorms have been suggested to be related to the gamma-rays from nuclear facilities (Torii et al., 2002), the updraft of the strong cold air under a cyclone (Diendorfer et al., 2006), winter monsoon (Chan et al., 2021), and the ionosphere (van der Velde et al., 2010). As yet, thunderstorms in Antarctica have not been reported, possibly due to the paucity of monitoring stations there (Holzworth et al., 2021). Polar thunderstorms are also related to global warming (Chen et al., 2021; Fang et al., 2022; Romps et al., 2014), which influences the hemispheric atmospheric circulation (Dethloff et al., 2006; Yuan & Martinson, 2000), where the convective heat results from the surface of ice sheets warmed via summer clouds (Perovich et al., 1999), and more water evaporation results from decreasing sea-ice coverage. In turn, the atmospheric moisture content and hydrological flux through thunderstorms affect both the global sea level change (GSLC) and greenhouse-gas emissions (GGE). However, the current assessment of the future of GSLC and GGE under climate change remains very uncertain. To improve their predictive accuracy, it is essential to establish a connection between ice sheet dynamics and the atmospheric physics. Our model that describes the ICF pertaining to thunderstorms implies that there is non-negligible interaction between the atmosphere and ice sheets. This work is the first to link the atmosphere to ice sheets by a thunderstorm. In this way, it is promising to better understand why winter and polar thunderstorms occur for further understanding of the atmospheric electrodynamics and thermodynamics for laboratory experiments on ICF. In addition to advances in understanding the atmospheric physics, this work sheds light on predicting future GSLC and GGE with a smaller uncertainty.

10991085, 2023, 12, Downloaded from https://onlinelibrary.wiley.com/doi/10.1002/hyp.15060 by Institution Of Atmospheric Physics, Wiley Online Library on [27/01/2024]. See the Terms and Conditions (https://onlinelibrary.wiley.com/terms-and-conditions) on Wiley Online Library for rules of use; OA articles are governed by the applicable Creative Commons License

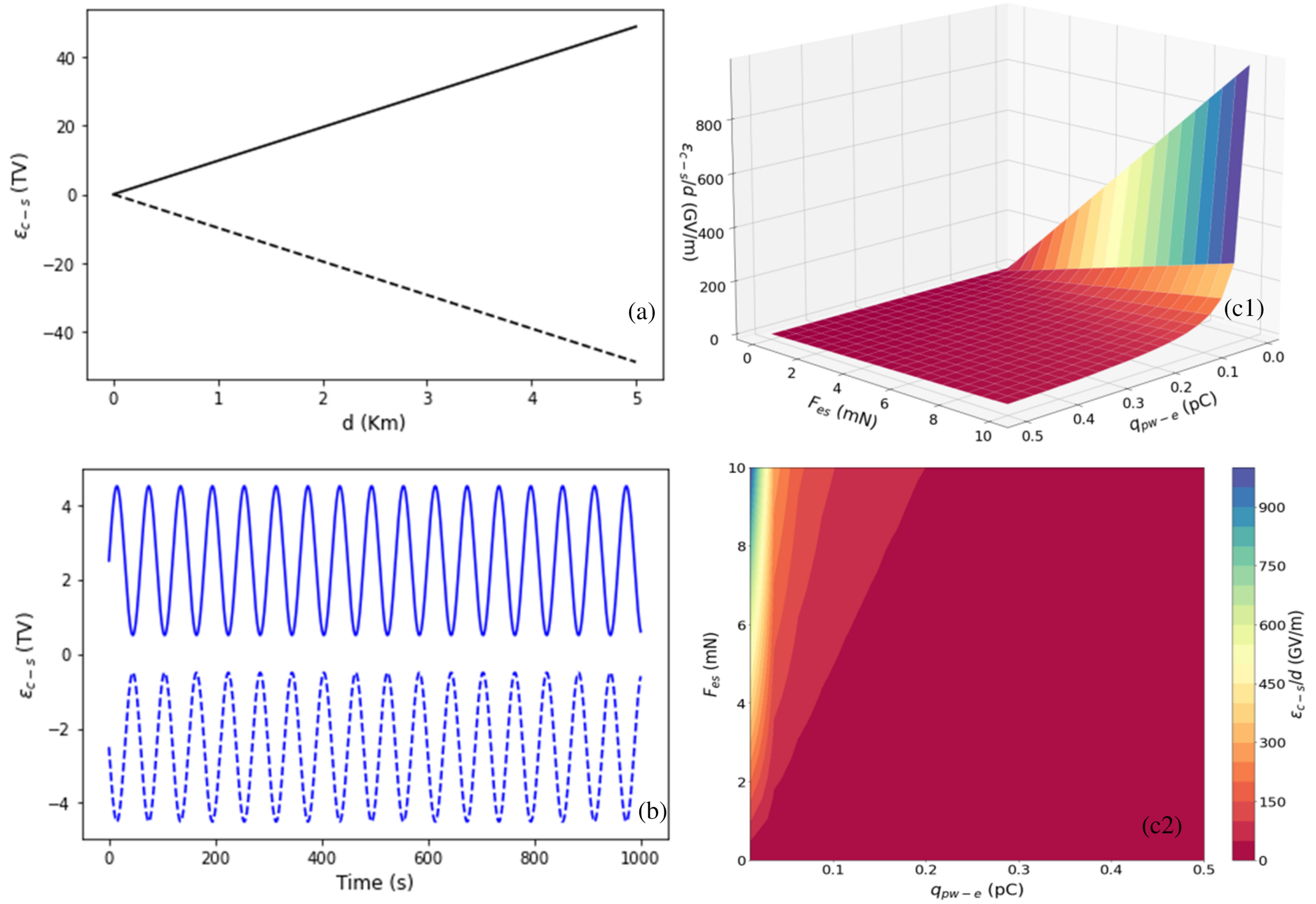

FIGURE 6 Relationships amidst the electric potential difference of cloud-to-ground, $\varepsilon_{c\text{-}s}$, the cloud base height, d, the electrostatic field force, F_{es}, and the amount of charges for individual pre-melted water droplet, $q_{pw\text{-}e}$. (a) is the relationship between $\varepsilon_{c\text{-}s}$ and d with a constant electro-thermo-coefficient. (b) is the relationship between $\varepsilon_{c\text{-}s}$ and d with a periodic electro-thermo-coefficient, using an equation $\varepsilon_{c-s} = c + d \times \sin(2\pi \times \omega \times t + \varphi)$, where c is the vertical shift with respect to the mid-line of $\varepsilon_{c-s} = \sin(2\pi \times \omega \times t)$, $=2.5$ Km, d is the amplitude, that is, the cloud base height, $=2$ Km, ω is the ordinary frequency (flashes/s, the number of the lighting flash per second), and φ is the phase in radians, $=0$. Note that the solid and dashed lines in (a) and (b) indicate the positive and negative value of $\varepsilon_{c\text{-}s}$, respectively. (c1) is the relationship of $\varepsilon_{c\text{-}s}/d$ to both F_{es} and $q_{pw\text{-}e}$ with a non-periodic electro-thermo-coefficient. (c2) is the contour lines of the values of $\varepsilon_{c\text{-}s}/d$ on the F_{es}–$q_{pw\text{-}e}$ plane as the colour bar. The mN, pC, GV/m, and TV indicate the milli-Newton, pico-Coulomb, Giga-Voltage/metre, and Tera-Voltage, respectively.

4 | CONCLUSIONS

The microstructural features typical of both depth hoar and ice-crust layers in blocks of snow and a firn core have been characterized using a micro-CT. For the depth hoar, the density is much lower, while the porosity and the pore sizes are greater than those in adjacent layers. For the ice-crusts, the density and the particle size are greater, while the porosity, the pore size, and the SSA are lower than those in adjacent layers. The DA of the depth hoar and adjacent layers indicate similar quasi-isotropic structures, probably because open voids are the predominant feature. Conversely, the DA of the ice-crust increases with increasing depth probably owing to the more heterogeneous pore distribution at greater depths.

For understanding the dynamic process of the ICF, we propose a model based on refreezing of electrostatically-transported PMW droplets by the electric field between thunderclouds and the ice sheets generated via a thunderstorm, together with related micro-structural parameters derived from the micro-CT data. Our model explains the typical characteristics of ice-crusts from their small thickness to their rapidity and low frequency of formation. Whether depth hoar forms within the ice-crust depends on both the kinetic energy (work) from the PMW droplets and the latent heat liberated from the freezing of the PMW.

Moreover, the dynamic process of the ICF is associated with the atmospheric physics using the formula $\varepsilon_{c\text{-}s}/d = F_{es}/q_{pw\text{-}e}$. To some degree, we provide an experimental geophysics-based method through studying ICF under laboratory conditions for learning more about winter and polar thunderstorms. This work is the first to build the relationship between the atmosphere and ice sheets involving a thunderstorm. Potentially, this method is also helpful to improve the predictive ability of future GSLC and GGE, aligning with the experimental understanding of both atmospheric circulation and hydrological cycle under climate change.

10991085, 2023, 12, Downloaded from https://onlinelibrary.wiley.com/doi/10.1002/hyp.15060 by Institution Of Atmospheric Physics, Wiley Online Library on [27/01/2024]. See the Terms and Conditions (https://onlinelibrary.wiley.com/terms-and-conditions) on Wiley Online Library for rules of use; OA articles are governed by the applicable Creative Commons License

ACKNOWLEDGEMENTS

This work was sponsored by the National Science Foundation of USA Arctic Natural Science grant (1603239). JY acknowledges support by the National Science Foundation of China (42071096), and the State Key Laboratory of Cryospheric Science (SKLCS-ZZ-2022). GH acknowledges support by the National Key R & D Program of China (2018YFA0605904). The authors thank Sergio H. Faria and Sepp Kipfstuhl for reviewing part of this manuscript. The authors thank Chris Polashenski, Zoe Courville and Lauren B. Farnsworth at CRREL for help with the firn core storage. The authors also acknowledge the use of the Ice Research Laboratory (Director-E.M. Schulson) at Dartmouth College.

CONFLICT OF INTEREST STATEMENT

The authors declare no conflicts of interest.

DATA AVAILABILITY STATEMENT

The data that support the findings of this study are available from the corresponding author upon reasonable request.

ORCID

Ian Baker https://orcid.org/0000-0001-6347-6960

REFERENCES

Alley, R. B. (2000). Ice-core evidence of abrupt climate changes. *Proceedings National Academy of Sciences United States of America*, *97*, 1331–1334.

Baker, M., & Dash, J. G. (1989). Charge transfer in thunderstorms and the surface melting of ice. *Journal of Crystal Growth*, *97*, 770–776.

Bartels-Rausch, T., Jacobi, H. W., Kahan, T. F., Thomas, J. L., Thomson, E. S., Abbatt, J. P. D., Ammann, M., Blackford, J. R., Bluhm, H., Boxe, C., Domine, F., Frey, M. M., Gladich, I., Guzmán, M. I., Heger, D., Huthwelker, T., Klán, P., Kuhs, W. F., Kuo, M. H., … Sodeau, J. R. (2014). A review of air-ice chemical and physical interactions (AICI): Liquids, quasi-liquids, and solids in snow. *Atmospheric Chemistry and Physics*, *14*, 1587–1633.

Batista, E. R., Xantheas, S. S., & Jonsson, H. (1998). Molecular multipole moments of water molecules in ice I*h*. *The Journal of Chemical Physics*, *109*, 4546–4551.

Battle, M. O., Severinghaus, J. P., Sofen, E. D., Plotkin, D., Orsi, A. J., Aydin, M., Montzka, S. A., Sowers, T., & Tans, P. P. (2011). Controls on the movement and composition of firn air at the West Antarctic Ice Sheet Divide. *Atmospheric Chemistry and Physics*, *11*, 11007–11021.

Boccippio, D. J. (2001). Lightning scaling relations revisited. *Journal of the Atmospheric Sciences*, *59*, 1086–1104.

Brooks, C. E. P. (1925). *The distribution of thunderstorms over the globe (No. 24)*. HM Stationery Office.

Caranti, J. M., & Illingworth, A. J. (1983). Transient Workman-Reynolds freezing potentials. *Journal of Geophysical Research: Oceans*, *88*(C13), 8483–8489.

Chan, P. W., Hon, K. K., & Li, Q. S. (2021). A rare winter thunderstorm event near Hong Kong. *Atmosfera*, *34*(4), 503–515.

Chen, Y., Romps, D. M., Seeley, J. T., Veraverbeke, S., Riley, W. J., Mekonnen, Z. A., & Randerson, J. T. (2021). Future increases in Arctic lightning and fire risk for permafrost carbon. *Nature Climate Change*, *11*, 404–410.

Dadic, R., Schneebeli, M., Lehning, M., Hutterli, M. A., & Ohmura, A. (2008). Impact of the microstructure of snow on its temperature: A model validation with measurements from Summit, Greenland. *Journal of Geophysical Research: Atmospheres*, *113*, D14303.

Das, S. B., & Alley, R. B. (2005). Characterization and formation of melt layers in polar snow: Observations and experiments from West Antarctica. *Journal of Glaciology*, *51*, 307–312.

Dash, J. G., Rempel, A. W., & Wettlaufer, J. S. (2006). The physics of premelted ice and its geophysical consequences. *Reviews of Modern Physics*, *78*, 695–741.

Deierling, W., Latham, J., Petersen, W. A., Ellis, S. M., & Christian, H. J., Jr. (2005). On the relationship of thunderstorm ice hydrometeor characteristics and total lightning measurements. *Atmospheric Research*, *76*, 114–126.

Dethloff, K., Rinke, A., Benkel, A., Køltzow, M., Sokolova, E., Kumar Saha, S., Handorf, D., Dorn, W., Rockel, B., von Storch, H., Haugen, J. E., Røed, L. P., Roeckner, E., Christensen, J. H., & Stendel, M. (2006). A dynamical link between the Arctic and the global climate system. *Geophysical Research Letters*, *33*, L03703.

Diendorfer, G., Kaltenbock, R., Mair, M., & Pichler, H. (2006). Characteristics of tower lightning flashes in a winter thunderstorm and related meteorological observations presented at International Lightning Detection Conference and International Lightning Meteorology Conference (ILDC/ILMC).

Fang, M., Li, X., Chen, H. W., & Chen, D. (2022). Arctic amplification modulated by Atlantic Multidecadal Oscillation and greenhouse forcing on multidecadal to century scales. *Nature Communications*, *13*, 1865.

Faria, S. H., Kipfstuhl, S., & Lambrecht, A. (2018). *The EPICA-DML deep ice core*. Springer.

Fegyveresi, J. M., Alley, R. B., Muto, A., Orsi, A. J., & Spencer, M. K. (2018). Surface formation, preservation, and history of low-porosity crusts at the WAIS Divide site, West Antarctica. *The Cryosphere*, *12*, 325–341.

Fletcher, N. (1968). Surface structure of water and ice, II. A revised model. *The Philosophical Magazine: A Journal of Theoretical Experimental and Applied Physics*, *18*, 1287.

Fourteau, K., Martinerie, P., Faïn, X., Schaller, C. F., Tuckwell, R. J., Löwe, H., Arnaud, L., Magand, O., Thomas, E. R., Freitag, J., & Mulvaney, R. (2019). Multi-tracer study of gas trapping in an East Antarctic ice core. *The Cryosphere*, *13*, 1–21.

Ganot, M., Yair, Y., Price, C., Ziv, B., Sherez, Y., Greenberg, E., Devir, A., & Yaniv, R. (2007). First detection of transient luminous events associated with winter thunderstorms in the eastern Mediterranean. *Geophysical Research Letters*, *34*, L12801.

Giddings, J. C., & LaChapelle, E. (1962). The formation rate of depth hoar. *Journal of Geophysical Research*, *67*, 2377–2383.

Gordon, M., & Taylor, P. (2009). The electric field during blowing snow events. *Boundary-Layer Meteorology*, *130*, 97–115.

Hobbs, P. V. (1974). *Ice physics* (1st ed.). Oxford University Press Inc.

Holzworth, R. H., Brundell, J. B., McCarthy, M. P., Jacobson, A. R., Rodger, C. J., & Anderson, T. S. (2021). Lightning in the Arctic. *Geophysical Research Letters*, *48*, e2020GL091366.

Jorgensen, L., & Madura, J. D. (1985). Temperature and size dependence for monte carlo simulations of tip4p water. *Molecular Physics*, *56*, 1381–1392.

Li, Y. (2023). Are bubbles in ice the potential space for hydrogen storage? *International Journal of Hydrogen Energy*, *50*(D), 575–585. https://doi.org/10.1016/j.ijhydene.2023.07.273

Li, Y., & Baker, I. (2021). Observations of the creep of polar firn. *Journal of Glaciology*, *10*, 1017.

Li, Y., & Baker, I. (2022a). Metamorphism observation and model of snow from Summit, Greenland under both positive and negative temperature gradients in a Micro CT. *Hydrological Processes*, *36*(9),e14696. https://doi.org/10.1002/hyp.14696

Li, Y., & Baker, I. (2022b). Dynamic observations of the densification of polar firn under compression using a micro-computed tomograph. *Journal of Geophysical Research: Earth Surface*, *126*, e2021JF006290.

10991085, 2023, 12, Downloaded from https://onlinelibrary.wiley.com/doi/10.1002/hyp.15060 by Institution Of Atmospheric Physics, Wiley Online Library on [27/01/2024]. See the Terms and Conditions (https://onlinelibrary.wiley.com/terms-and-conditions) on Wiley Online Library for rules of use; OA articles are governed by the applicable Creative Commons License

Li, Y., Keegan, K., & Baker, I. (2023). Observations of the creep of polar firn at different temperatures. *Cold Regions Science and Technology* (Revised).

Louden, P. B., & Gezelter, J. D. (2017). Friction at ice Ih/water interfaces is governed by solid/liquid hydrogen-bonding. *The Journal of Chemical Physics*, *121*, 26764–26776.

Lu, Y., & Chen, J. (2021). Adjustable diffusion enhancement of water molecules in a nanoscale water bridge. *Nanoscale*, *13*, 1000–1005.

Mansell, E. R., MacGorman, D. R., Ziegler, C. L., & Straka, J. M. (2005). Charge structure and lightning sensitivity in a simulated multicell thunderstorm. *Journal of Geophysical Research*, *110*, D12101.

Mitchell, L. E., Buizert, C., Brook, E. J., Breton, D. J., Fegyveresi, J., Baggenstos, D., Orsi, A., Severinghaus, J., Alley, R. B., Albert, M., Rhodes, R. H., McConnell, J. R., Sigl, M., Maselli, O., Gregory, S., & Ahn, J. (2015). Observing and modeling the influence of layering on bubble trapping in polarfirn. *Journal of Geophysical Research – Atmospheres*, *120*, 2558–2574.

Perovich, D. K., Andreas, E. L., Curry, J. A., Eiken, H., Fairall, C. W., Grenfell, T. C., Guest, P. S., Intrieri, J., Kadko, D., Lindsay, R. W., & McPhee, M. G. (1999). Year on ice gives climate insights. *Eos, Transactions American Geophysical Union*, *80*, 481.

Pfalzgraff, W. C., Neshyba, S., & Roeselová, M. (2011). Comparative molecular dynamics study of vapor-exposed basal, prismatic and pyramidal surfaces of ice. *The Journal of Physical Chemistry. A*, *115*, 6184–6193.

Romps, D. M., Jacob, T., Seeley, D. V., & Molinari, J. (2014). Projected increase in lightning strikes in the United States due to global warming. *Science*, *346*(6211), 851–854.

Schmidt, D. S., & Dent, J. D. (1993). A theoretical prediction of the effects of electrostatic forces on saltating snow particles. *Annals of Glaciology*, *18*, 234–238.

Schmidt, D. S., Dent, J. D., & Schmidt, R. A. (1998). Charge-to-mass ratio of individual blowing-snow particles. *Annals of Glaciology*, *26*, 207–211.

Sommer, C. G., Lehning, M., & Fierz, C. (2018). Wind tunnel experiments: Influence of erosion and deposition on wind-packing of new snow. *Frontiers in Earth Science*, *6*(4), 1.

Sommer, C. G., Wever, N., Fierz, C., & Lehning, M. (2018). Investigation of a wind-packing event in Queen Maud Land, Antarctica. *The Cryosphere*, *12*, 2923–2939.

Szabo, D., & Schneebeli, M. (2007). Subsecond sintering of ice. *Applied Physics Letters*, *90*, 151916.

Tang, F., Ohto, T., Sun, S., Rouxel, J. R., Imoto, S., Backus, E. H. G., Mukamel, S., Bonn, M., & Nagata, Y. (2020). Molecular structure and modeling of water-air and ice-air interfaces monitored by sum-frequency generation. *Chemical Reviews*, *120*, 3633–3667.

Torii, T., Takeishi, M., & Hosono, T. (2002). Observation of gamma-ray dose increase associated with winter thunderstorm and lightning activity. *Journal of Geophysical Research*, *107*(D17), ACL 2-1-13.

van der Velde, O. A., Bor, J., Li, J., Cummer, S. A., Arnone, E., Zanotti, F., Füllekrug, M., Haldoupis, C., NaitAmor, S., & Farges, T. (2010). Multi-instrumental observations of a positive gigantic jet produced by a winter thunderstorm in Europe. *Journal of Geophysical Research*, *115*, D24301.

Vrbka, L., & Jungwirth, P. (2005). Brine rejection from freezing salt solutions: A molecular dynamics study. *Physical Review Letters*, *95*, 148501.

Wang, D., Wu, T., & Takagi, N. (2018). Charge structure of winter thunderstorm in Japan: A review and an update. *IEEJ Transactions on Power and Energy*, *138*(5), 310–314.

Wang, Z. (2014). *Thermodynamics*. Peiking University Press.

Weinhart, A. H., Kipfstuhl, S., Hörhold, M., Eisen, O., & Freitag, J. (2021). Spatial distribution of crusts in Antarctic and Greenland snowpack and implications for snow and firn studies. *Frontiers in Earth Science*, *10*, 3389.

Wettlaufer, J. S. (1999). Impurity effects in the premelting of ice. *Physical Review Letters*, *82*, 2516–2519.

Williams, E., Mushtak, V., Rosenfeld, D., Goodman, S., & Boccippio, D. (2005). Thermodynamic conditions favorable to superlative thunderstorm updraft, mixed phase microphysics and lightning flash rate. *Atmospheric Research*, *76*, 288–306.

Winarto, Takaiwa, D., Yamamoto, E., & Yasuoka, K. (2015). Structures of water molecules in carbon nanotubes under electric fields. *The Journal of Chemical Physics*, *142*, 124701.

Winarto, Yamamoto, E., & Yasuoka, K. (2017). Water molecules in a carbon nanotube under an applied electric field at various temperatures and pressures. *Water*, *9*, 473.

Winebrenner, D.P., Arthern, R.J. & Shuman, C.A. (2001). Mapping Greenland accumulation rates using observations of thermal emission at 4.5-cm wavelength. *Journal of Geophysical Research – Atmosphere*, *106* (D24), 33919–33934.

Yuan, X. J., & Martinson, D. G. (2000). Antarctic sea ice extent variability and its global connectivity. *Journal of Climate*, *13*, 1697–1717.

Zheng, D., Wang, D., Zhang, Y., Wu, T., & Takagi, N. (2019). Charge regions indicated by LMA lightning flashes in Hokuriku's winter thunderstorms. *Journal of Geophysical Research – Atmospheres*, *124*, 7179–7206.

How to cite this article: Li, Y., Fu, C., Keegan, K., Yang, J., Huang, G., & Baker, I. (2023). Microstructural characterization of depth hoar and ice-crust layers using a micro-CT, and hypothesis of ice-crust formation under a thunderstorm. *Hydrological Processes*, *37*(12), e15060. https://doi.org/10.1002/hyp.15060

10991085, 2023, 12, Downloaded from https://onlinelibrary.wiley.com/doi/10.1002/hyp.15060 by Institution Of Atmospheric Physics, Wiley Online Library on [27/01/2024]. See the Terms and Conditions (https://onlinelibrary.wiley.com/terms-and-conditions) on Wiley Online Library for rules of use; OA articles are governed by the applicable Creative Commons License